Sb-induced reconstructions on Si(113): Adatoms as the key elements

M. Siebert,* Th. Schmidt, J. I. Flege, and J. Falta
Institut für Festkörperphysik, Universität Bremen, Postfach 330440, D-28334 Bremen, Germany
(Received 21 January 2005; revised manuscript received 2 May 2005; published 13 July 2005)

The adatom site is identified and determined as the main structural element of Sb-induced surface reconstructions of Si(113) by means of x-ray standing waves, x-ray photoelectron spectroscopy, and low-energy electron diffraction (LEED) in combination with density functional theory calculations. The analysis yields that the Sb adatom site can be found prevalently at Sb coverages below 1 ML. With increasing coverage, the relative amount of Sb residing in adatom sites is reduced in favor of mainly Sb tetramer formation, leading to a complex mixture of (2×2) reconstructions at coverages above 1 ML. The observation of (1×2) LEED patterns can be explained by the formation of small antiphase domains of (2×2) reconstructions. Upon annealing, partial desorption of Sb leads to the formation of a missing-row structure with a $(1\times n)$ LEED pattern.

DOI: 10.1103/PhysRevB.72.045323 PACS number(s): 68.18.Fg, 68.43.Bc, 68.43.Fg, 68.49.Uv

I. INTRODUCTION

The detailed understanding of the adsorption of group V elements on silicon surfaces has attracted much interest in the past years as these elements are promising candidates for the surfactant mediated epitaxy (SME) of germanium on silicon and the passivation of silicon surfaces.[1] Without application of a surfactant, Ge growth proceeds in the Stranski-Krastanov mode by the formation of three-dimensional islands. This growth mode is driven by the lattice mismatch of 4.2%.

On the Si(001) surface—the substrate most commonly used for semiconductor applications—Stranski-Krastanov growth of Ge can be suppressed by preadsorption of 1 monolayer (ML) of arsenic; however, many defects were found in the Ge film above a coverage of 12 ML.[2] Distinctively, on Si(111) high quality Ge films can be grown by applying Sb as a surfactant.[3] However, the Si(111) surface is of less technological importance merely due to the poor quality of the oxide layers. As the truncated idealized Si(113) surface is formed by alternating rows of Si(001)-like and Si(111)-like atoms, it shows characteristics of both the Si(001) and the Si(111) surface. Moreover, excellent oxide films have been achieved on the Si(113) surface.[4] Thus, the Si(113) surface can be regarded as a promising candidate for SME of Ge on silicon and hence may be applied to the application in the production of semiconductor devices. From the experience with SME on Si(111), Sb is one of the most promising candidates for SME on Si(113).

Preceding to an investigation and optimization of SME it is necessary to obtain a detailed understanding of the adsorption process. Up to now, Sb covered Si(113) surfaces were investigated with scanning tunneling microscopy in combination with density functional theory (DFT) calculations[5,6] and with x-ray photoelectron spectroscopy (XPS) and low-energy electron diffraction (LEED).[7] For coverages below 1 ML, it was proposed that adatom sites are found in antiphase domain boundaries of (1×1) periodicity between (2×2) domains.[6] For coverages between 1 ML and 1.5 ML, Wolff *et al.*[5] suggested that (2×2) Sb adatom-tetramer reconstructions are formed. Later, authors from the same group (Dąbrowski *et al.*[6]) drew conclusions on interstitial dimer structures and argued that the dimers contain Sb or Si atoms depending on the Sb coverage.

In this paper, we present the results of XPS, Auger electron spectroscopy (AES), and LEED studies for different Sb coverages on the Si(113) surface in order to develop a structural phase diagram. Employing x-ray standing waves (XSW) and DFT, the atomic structure of the Sb-induced reconstructions is investigated in detail.

II. EXPERIMENTAL AND COMPUTATIONAL DETAILS

All experiments were carried out at the undulator beamline BW1 at the Hamburg synchrotron radiation laboratory (HASYLAB). A standard nondispersive monochromator setup using pairs of symmetrically and asymmetrically cut crystals was applied in order to perform XSW measurements in (111) and (113) Bragg reflection. Additionally, XSW measurements were performed dispersively[8] in (202) Bragg reflection with a Si(113) monochromator setup.

For the XSW measurements, photoelectron data were recorded with an energy-dispersive electron analyzer while tuning the incident photon energy through the Bragg condition. The photoelectron yield was evaluated according to the dynamical theory of diffraction as described by Batterman and Cole.[9] The photoelectron yield can be expressed[10,11] as a function of the incident energy with the coherent fraction f_c and the coherent position Φ_c. f_c and Φ_c are the modulus and phase of the (hkl) Fourier component of the distribution function of the ensemble of atoms that contributes to the photoelectron signal under consideration

$$f_c^{hkl}\exp(2\pi i\Phi_c^{hkl}) = \frac{1}{N}\sum_{n=1}^{N} D_n^{hkl}\exp(i\vec{H}\vec{r}_n). \qquad (1)$$

Here, $\vec{H}$ is the scattering vector related to the (hkl) Bragg condition, and the sum is carried out over all N atoms of the ensemble that are located at $\vec{r}_n$. The Debye-Waller factors D_n^{hkl} account for thermal vibrations around these equilibrium

positions. From Eq. (1) it is evident that only the noninteger part of Φ_c is physically relevant.

All samples were investigated under UHV conditions with a base pressure of 1×10^{-10} mbar. After RCA cleaning,[12] the samples were degassed in the UHV chamber for at least 14 h at temperatures between 600 °C and 650 °C by applying direct current through the sample. Subsequently, the protective oxide layer was removed by heating to a temperature of 870 °C for 5 min. Rapid temperature changes were avoided in order to maintain a crystal quality sufficient for XSW experiments. The temperatures were recorded with an infrared pyrometer with an estimated absolute uncertainty of ±50 °C. With LEED the (3×2) reconstruction of a clean Si(113) surface[13] was verified. Sb was deposited from a Knudsen cell at different substrate temperatures with a deposition rate larger than 0.1 ML/min. Here and in the following, 1 ML=4.1×10^{14} cm^{-2}. In order to determine the Sb coverage, XPS spectra of Si-1*s* and Sb-$2p_{3/2}$ photoelectrons were recorded at an incident photon energy of 4.5 keV. Attenuation effects on the Si-1*s* electron signal by the Sb film can be neglected for coverages of concern in this context. The absolute Sb coverage was determined with a relative uncertainty of 25% by measuring the relative XPS ratio of the Si-1*s* and Sb-$2p_{3/2}$ intensities, as will be described in detail in Sec. III.

Structural calculations were performed using the density-functional theory of Hohenberg, Kohn, and Sham,[14,15] as incorporated into the package PWscf by Baroni and co-workers.[16] The electron-ion interaction is considered in the form of *ab initio* norm-conserving pseudopotentials,[17,18] while the electron-electron interaction is treated within the local-density approximation.[19,20] Self-consistent solutions to the Kohn-Sham equations were obtained by employing a converged $\vec{k}$ point grid of $(4\times4\times1)$ in the surface Brillouin zone according to the scheme proposed by Monkhorst and Pack.[21] The single-particle wave functions were expanded using a plane-wave basis up to a kinetic energy cutoff of 25 Ry. With respect to convergence of the total energy, reliable surface structures may already be obtained at cutoff energies, of around 14 Ry. However, with further increased cutoff energies, subtle relaxation effects in the near-surface region were still observed. These small changes in the coordinates of the Sb and Si atoms add up in the calculation of the Fourier coefficients in the XSW calculations since the reference for the XSW signal is the Si bulk, i.e., the bottom Si bilayer atoms held fixed at their corresponding bulk positions. Hence, in this case, the convergence of the XSW Fourier coefficients with respect to the employed high-energy cutoff level poses a sharper criterion for convergence than the standard convergence test for the cutoff energy. Therefore, an increased energy cutoff level of at least 20 Ry was used, which was found to be appropriate in order to fulfill this additional criterion.

III. PHASE DIAGRAM

In order to establish a structural phase diagram, several monolayers of Sb were deposited on the clean Si(113) surface at RT. Subsequently, the samples were repeatedly annealed for 2 min at increasingly higher *T*. XPS and LEED data were recorded at RT after each annealing cycle. The results are presented in Fig. 1.

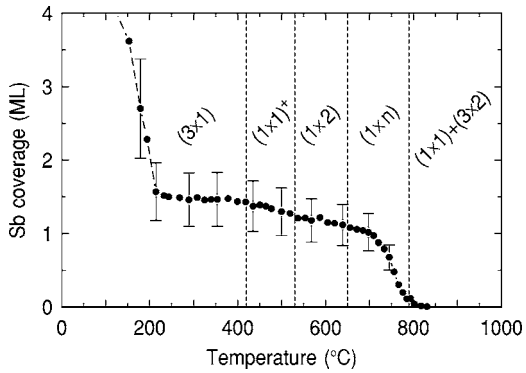

FIG. 1. Sb coverage as a function of the annealing temperature. Additionally, changes in the surface reconstruction as observed with LEED after cooling down to RT are labeled. Initially, several ML of Sb were desposited at RT for which a diffuse LEED pattern was recorded.

Similar experiments have already been performed by An *et al.*[7] For an initial coverage of several monolayers of Sb, these authors report on a change in the LEED from a diffuse pattern at RT via a diffuse (1×1) LEED pattern between 200 °C and 400 °C to a clear (1×1) pattern at 400 °C. By further annealing, a (1×2) reconstruction was observed at 500 °C with additional weak and diffuse $\left(\frac{1}{2}n\right)$ peaks evolving to a (2×2) reconstruction at 700 °C. After annealing at 800 °C a (2×5) reconstruction was found.

These authors also reported a (3×1) reconstruction with diffuse $\left(\frac{1}{3}n\right)$ peaks after RT deposition of what they assumed to be 2 ML. This coverage was obtained by tentatively estimating a coverage of 2 ML at an annealing temperature of $T=400$ °C. However, our calibration reveals a coverage of 1.43 ± 0.36 ML of Sb at this annealing temperature. This was accomplished by annealing experiments monitored by AES and comparison to the AES signal of a Si(111) sample on which Sb was deposited at a temperature of 600 °C. It is well known that this preparation results in a $(\sqrt{3}\times\sqrt{3})$ reconstruction at a coverage of 1 ML Sb.[22] For the coverage calibration of the XPS signal of the Si(113) sample, the mean values of the XPS and AES intensities at the plateaus were used, as established during the experiments of stepwise annealing.

To a large extent, our LEED data agree with the data presented by An *et al.*;[7] however, we also observed significant differences that we will explain in the following. By annealing from RT to 400 °C we found a (3×1) pattern with faint $\left(\frac{1}{3}n\right)$ peaks. A similar LEED pattern was reported by An *et al.* only for a low initial coverage. This difference may be attributed to different annealing periods showing that the resulting configurations are very sensitive to preparational parameters. The (1×1) pattern, which is marked in Fig. 1 as $(1\times1)^+$, is similar to the observation of An *et al.* However, at $T=500$ °C, we observed a change in the LEED pattern to a (1×2) reconstruction with weak and diffuse $\left(n\frac{1}{2}\right)$ peaks instead of a clear (2×2) pattern. By further annealing to $T=650$ °C, the $\left(n\frac{1}{2}\right)$ peaks became more intense. The different

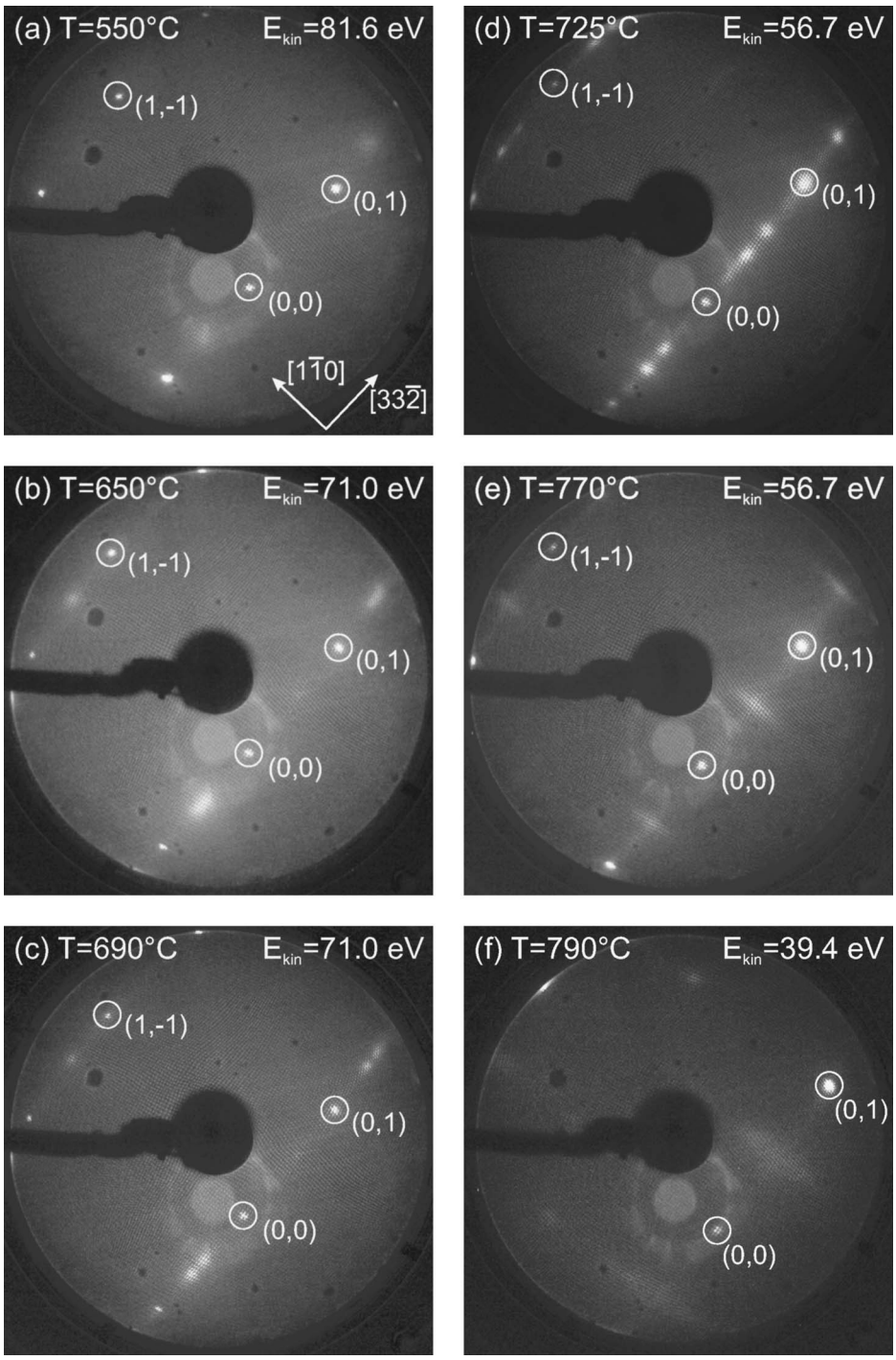

FIG. 2. LEED patterns recorded after RT deposition of several ML Sb and subsequent annealing at (a) 550 °C, (b) 650 °C, (c) 690 °C, (d) 725 °C, (e) 770 °C, and (f) 790 °C. The position of the integral order spots is indicated.

findings for the LEED patterns in this temperature region may be explained by the formation of antiphase boundaries in the $[1\bar{1}0]$ direction between local patches of small (2×2) domains in our experiments.

Figure 2 shows the LEED patterns that were recorded after annealing to temperatures above $T=500$ °C with smaller temperature steps than performed in the work by An *et al.*[7] A close investigation yields that the diffuse $(n\frac{1}{2})$ peaks split into multiple peaks in the $[33\bar{2}]$ direction with increasing temperature up to $T=725$ °C.

At an annealing temperature of 690 °C the two central peaks of a (1×7) pattern have evolved in the LEED pattern [Fig. 2(c)]. At 725 °C, a (1×5) pattern has fully developed [Fig. 2(d)]. As integral order peaks do not split, faceting can be excluded and the variation of the LEED pattern can be assigned to the formation of $(1\times n)$ superstructures, dominated by a (1×7) or a (1×5) reconstruction, respectively. Hence, the LEED pattern in Fig. 2(b) can be explained by the presence of a $(1\times n)$ superstructure with high n. Upon further annealing, the LEED becomes a (1×2) pattern with weak and diffuse half-order spots. These spots are broadened in $[33\bar{2}]$ and streaky in $[1\bar{1}0]$ direction, which can be seen in Fig. 2(e). At 790 °C, these spots have almost vanished and

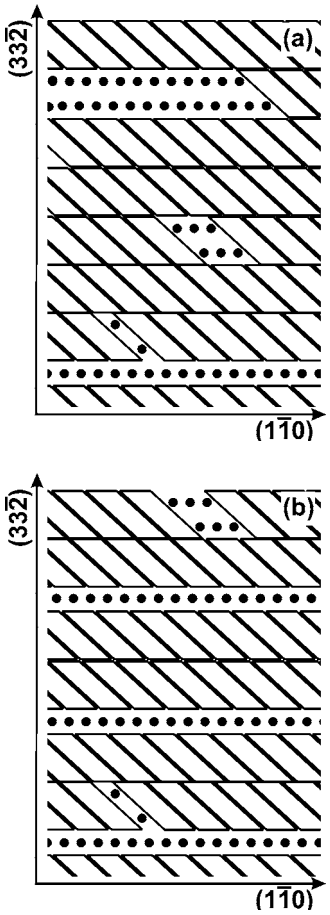

FIG. 3. Illustration of the formation of Sb vacancy rows. Parallelograms represent (2×2) reconstructed areas and dots represent (1×1) reconstructed elements. Several antiphase domain boundaries in the $[1\bar{1}0]$ direction are indicated. (a) The initial formation of Sb vacancy rows at large distances in the $[33\bar{2}]$ direction. (b) A higher density of vacancy rows forming a (1×5) superstructure.

the LEED changes to a (1×1) pattern with weak additional spots of a (3×2) pattern [Fig. 2(f)].

The transition of the LEED pattern from a (1×2) via a (1×7), a (1×5) and a (1×2) to a $(1\times1)+(3\times2)$ pattern can be explained by the formation of Sb vacancy rows along the $[1\bar{1}0]$ direction as illustrated in Fig. 3.

At the beginning of the formation of this network, the distances between missing rows are very large and irregular, which is indicated by the $(1\times n)$ pattern in Fig. 2(b) and sketched in Fig. 3(a). With increasing annealing temperature, the coverage decreases and the distances between the rows are reduced. The contribution of patterns with higher n weakens in benefit of reconstructions with lower n like the (1×7), and subsequently the (1×5) evolves [Fig. 3(b)]. Moreover, with a decreasing distance between the missing rows, an increasing interaction between the rows is expected resulting in a better ordering and hence sharper LEED spots. Within this model, the two central peaks [i.e., those close to the $(n\frac{m}{2})$ position] are expected to be more intense due to the underlying (2×2) periodicity, which is in agreement with the experimental findings.

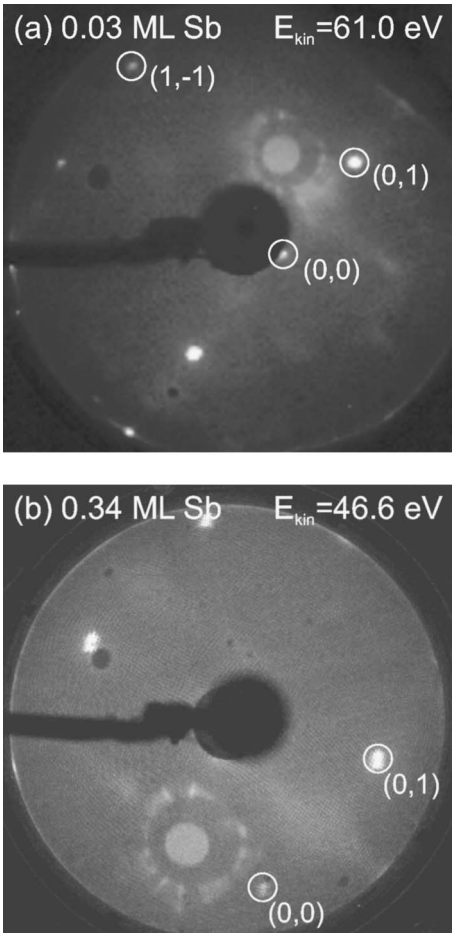

FIG. 4. (a) (1×1) LEED pattern of a sample with 0.03 ML Sb coverage with faint (3×2) contribution. (b) (1×2) LEED pattern of a sample with 0.34 ML Sb coverage. The $(n\frac{1}{2})$ peaks are streaky.

For annealing temperatures above 770 °C, the half-order spots broaden and weaken in intensity. This points to the formation of very small (2×2) domains [Fig. 2(e)]. Successively, a $(1\times1)+(3\times2)$ pattern is formed as found for a Sb coverage of 0.12 ML [Fig. 2(f)]. A comparable (1×1) LEED pattern can also be achieved by depositing small amounts of Sb on the Si(113) surface at an elevated temperature of 500–600 °C, which is shown in Fig. 4(a) and discussed below for 0.03 ML Sb deposition. The fact that such a small amount of adsorbed Sb leads to the almost complete disappearance of the (3×2) pattern indicates that Sb strongly destabilizes the (3×2) reconstruction, which is in contrast to a report by Wolff *et al.*[5]

In the following section, we will address the question whether a (1×1) structural element exists that could be a stable building block for a large variety of Sb-induced reconstructions on the Si(113) surface. For this purpose, thorough XSW and DFT studies were performed for the initial stages of Sb adsorption.

IV. XSW MEASUREMENTS AND DFT CALCULATIONS

A. Sb coverages below 1 ML

Figure 5 shows the XSW spectra of a sample after deposition of 0.03 ML Sb at 600 °C resulting in a sharp (1×1)

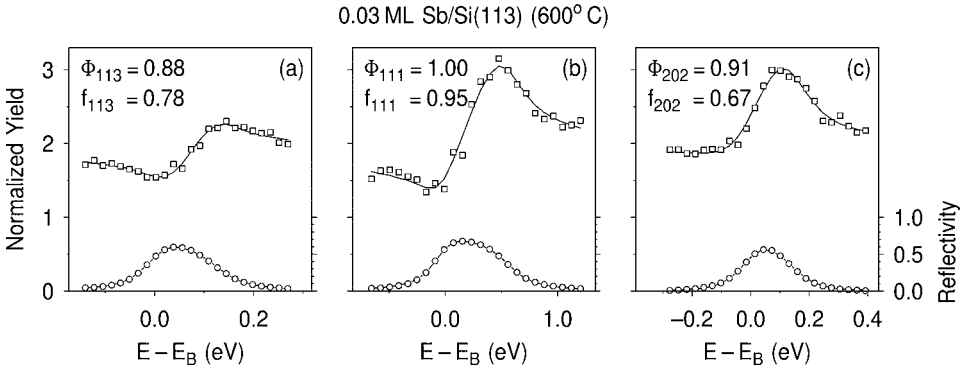

FIG. 5. XSW data and fit (solid lines) of reflectivities (○) and photoelectron yield (□) at a photon energy of $E=4.5$ keV in (a) (111), (b) (113), and (c) (202) reflection geometry. The photoelectron yield is shifted by +1 for display purposes. The Sb coverage is 0.03 ML.

LEED pattern with faint remainders of a (3×2) pattern [Fig. 4(a)].

The obtained coherent fractions f_c of all Bragg reflections are high. The deviation of the coherent fraction $f_c^{111}=0.95\pm0.02$ from unity is so small that it could be fully assigned to the influence of the Debye-Waller factor. The values for $f_c^{113}=0.78\pm0.02$ and $f_c^{202}=0.67$ show that the surface is dominated by a single adsorption site and only marginal contributions of additional sites are to be taken into account. The measurements in (202) Bragg geometry were obtained using a (113) monochromator. In a dispersive setup, additional parameters are demanded for the data evaluation.[8] As these parameters strongly affect the deduced coherent fraction f_c, the determination of f_c is less accurate than for nondispersive measurements. Therefore, the values obtained for f_c^{202} are less reliable than those for f_c^{111} and f_c^{113}, and f_c^{202} is not considered for further evaluation. From the values of f_c^{111} and f_c^{113}, we thus conclude that the photoelectron yield is mainly dominated by a *single* adsorption site. However, the determination of Φ_c for XSW data taken in a dispersive setup is less affected by these experimental uncertainties. Hence, this value can be regarded more reliable and has thus been used for the determination of the Sb adsorbate structure.

Figure 6 shows the XSW spectra of a sample on which 0.34 ML Sb was deposited at $T=500$ °C and which shows a (1×2) LEED pattern with weak and diffuse $(n\frac{1}{2})$ peaks [Fig. 4(b)].

The coherent fraction f_c^{113} is practically identical and f_c^{111} is insignificantly decreased with respect to the results obtained for 0.03 ML. Hence, this surface can also be described by a single adsorption site that mainly determines the photoelectron yield. A comparison of the coherent positions Φ_c is presented in Table I, which shows that the coordinates of the proposed single adsorption site vary only within the uncertainty of the measurements. Thus, this adsorption site is conserved although the coverage was increased and changes in the LEED pattern were observed. Hence, it is reasonable to evaluate the averaged coherent positions of the investigated coverages as shown in Table I in order to determine the main site by triangulation directly. This procedure yields an adsorption site that is compatible with a (1×1) surface reconstruction as observed with LEED. A model of such a reconstruction is shown in Fig. 7.

In accordance with Wolff *et al.*[5] we denote it as the *Antimony-adatom* site.

In order to investigate the Sb-adatom-induced relaxation of the Si surface atoms, the XSW data were compared to DFT calculations. For a further refinement of the analysis and for investigations at higher coverages, additional building blocks for surface reconstructions have been inspected and will be discussed below. A repeated-slab geometry with a vacuum region equivalent of 9 Si bilayers (BL) in thickness was constructed for all calculations. The (1×1) unit cell consists of 1 atomic layer of Sb atoms and 12 Si layers underneath with the bottom 2 layers fixed at bulklike positions, while all the other atoms were allowed to relax into their minimum-energy positions. In order to simulate the XSW data of the resulting adsorbate geometries, the bulklike silicon bilayer was chosen as a reference to compute the coherent positions.

A comparison of rows 3 and 6 in Table I shows that the differences between the averaged measured and the calculated Φ_c of a (1×1) reconstruction are within the accuracy of the measurements and thus in excellent agreement. The experimentally determined site is defined with respect to the Si bulk diffraction planes, whereas the calculated site results from *ab initio* DFT calculations. As they are completely in-

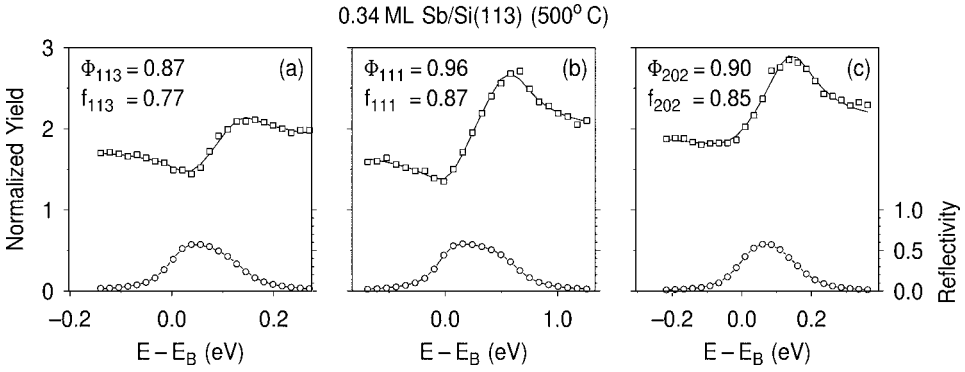

FIG. 6. XSW data and fit (solid lines) of reflectivities (○) and photoelectron yield (□) at a photon energy of $E=4.5$ keV in (a) (111), (b) (113), and (c) (202) reflection geometry. The photoelectron yield is shifted by +1 for display purposes. The Sb coverage is 0.34 ML.

TABLE I. Overview over measured and calculated coherent positions Φ_c^{hkl} and fractions f_c^{hkl}. The uncertainty of the measurement $\Delta\Phi_c$ is in the order of ±0.02. The calculated values result from DFT for possible surface reconstructions.

	Φ_c^{111}	Φ_c^{113}	Φ_c^{202}	f_c^{111}	f_c^{113}	f_c^{202}
XSW @ 0.03 ML Sb	1.00	0.88	0.91	0.95	0.78	0.67
XSW @ 0.34 ML Sb	0.96	0.87	0.90	0.87	0.77	0.85
XSW (low coverage average)	0.98	0.88	0.91	0.91	0.78	0.76
XSW @ 1.26 ML Sb	0.97	0.93	0.91	0.67	0.58	0.71
XSW @ 1.59 ML Sb	0.95	1.01	0.89	0.41	0.38	0.55
DFT Sb adatom (1×1)	0.96	0.85	0.91	1.00	1.00	1.00
DFT Si-Si dimer (2×2)	0.96	0.94	0.95	0.92	0.92	1.00
DFT Sb-Si dimer (2×2)	0.94	0.96	0.94	0.55	0.86	1.00
DFT Sb-Sb dimer (2×2)	0.89	0.98	0.91	0.31	0.78	0.87
DFT Sb adatoms+tetramers(2×2)	1.02	1.13	1.08	0.52	0.36	0.56
DFT Sb tetramers (2×2)	0.11	0.23	0.18	0.43	0.84	0.84

dependent, the excellent agreement of the coherent positions Φ_c confirms the adatom site.

Because of the high coherent fractions, contributions of additional sites can only be marginal; therefore, we conclude that the Sb adatom site is prevalent for coverages up to 0.34 ML. An overview of the calculated Sb adatom surface configuration and the bond lengths is given in Fig. 7. The bond lengths between the Sb and Si surface atoms were calculated to 2.64 Å for bonds to Si(001)-like atoms and to 2.88 Å for bonds to Si(111)-like atoms. For Sb/Si(111) an Sb-Si bond length of 2.66 Å was determined with surface extended x-ray absorption fine structure.[23] Hence, we conclude that the bonds of the Sb adatoms to the Si(111)-like atoms are significantly stretched. Thus, high tensile strain is induced in the $[33\bar{2}]$ direction on the Si surface. The bonds between the Si(111)-like and Si(001)-like surface atoms have a length of 2.55 Å in comparison to the Si-Si bulk value of 2.35 Å. Therefore, they are likely to be broken with increasing coverage and the formation of interstitial Sb or Si dimers may result from this process.[6,24] At a coverage of 0.34 ML, most likely Si-Si dimers may be found, which will be confirmed by the investigations in Sec. IV B. The analysis of the bond lengths in a (2×2) Si-Si dimer structure as resulting from DFT (see Fig. 8) yields Sb-Si bond lengths between 2.57 Å and 2.64 Å.

Hence, surface strain is significantly relaxed as compared to a (1×1) adatom reconstruction. Though all Sb atoms reside in adatom sites, the calculated coherent fractions $f_c^{111}=0.92$ and $f_c^{113}=0.92$ are different from unity. This implies that Sb adatoms in this (2×2) unit cell occupy slightly different positions and thus are not exactly equivalent, due to their different locations with respect to the dimer. Nevertheless, the Sb Fourier coefficients determined by DFT for (1×1) Sb adatom and (2×2) Si-Si dimer structures differ

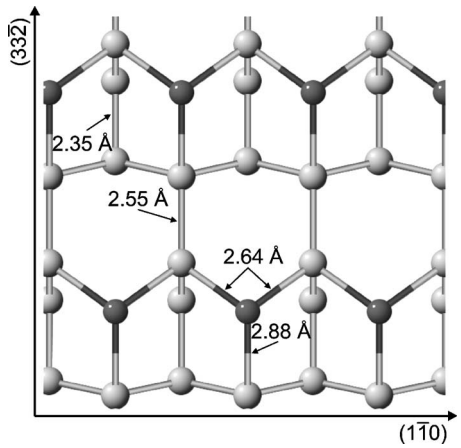

FIG. 7. Model of the adatom reconstruction of Sb on a Si(113) surface as resulting from XSW measurement and DFT calculations. Sb atoms are displayed in dark shade and Si atoms in light shade. The measured and the calculated Sb adatom position is virtually identical.

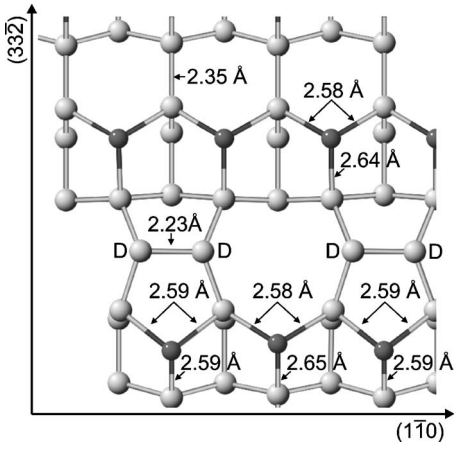

FIG. 8. (2×2) Sb adatom reconstruction with interstitial Si dimers as resulting from DFT. Sb atoms are displayed in dark shade and Si atoms in light shade. Si atoms that are part of a dimer are marked with *D*. The bond length 2.35 Å between Si(001)-like and Si(111)-like surface atoms equals the Si-Si bulk value and the Sb-Si bond lengths vary between 2.57 Å and 2.64 Å.

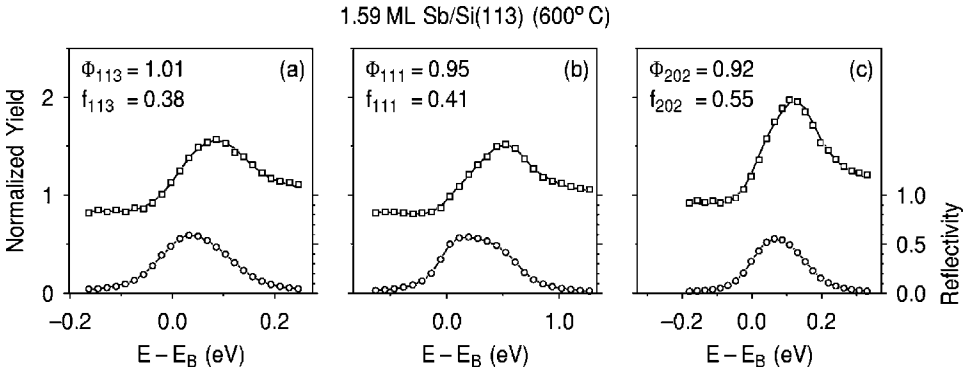

FIG. 9. XSW data and fit (solid lines) of reflectivities (○) and photoelectron yield (□) at a photon energy of $E=4.5$ keV in (a) (111), (b) (113), and (c) (202) reflection geometry. The photoelectron yield is shifted by +1 for display purposes. The Sb coverage is 1.59 ML.

only marginally from each other. Judging from the observed LEED pattern and due to Sb adatom induced surface strain, a small but significant contribution of (2×2) Si-Si dimers should be taken into account for the sample at 0.34 ML.

B. Sb coverages above 1 ML

XSW measurements of samples with coverages of 1.26 ML and 1.59 ML as determined by AES analysis were performed. The results are presented in Table I, and the exemplary XSW data of the sample with a coverage of 1.59 ML is shown in Fig. 9. The LEED patterns of both samples are in accordance with the investigations presented in Sec. III.

The coherent positions Φ_c of the two samples are only slightly changed in comparison to the respective values for the low coverage samples. This suggests that at higher coverages, the Sb adatom site is the key structural element. Nevertheless, the coherent fractions f_c are lowered in all Bragg reflections as compared to the samples with coverages below 0.34 ML, hence additional adsorption sites need to be considered. The decrease of the coherent fractions f_c with increasing coverage indicates a progressive occupation of additional sites.

For coverages above 1 ML, several structures were reported and Dąbrowski *et al.*[6] suggested that several phases may coexist. Thus, we performed DFT calculations for mixed Sb-Si dimers,[6] Sb-Sb dimers,[6] Sb adatom tetramer,[5] and Sb tetramer[5] reconstructions in addition to the previously discussed Sb adatom and Si-Si dimer reconstructions.

The Sb-Si and Sb-Sb dimer structures can be derived from the structure displayed in Fig. 8 by substituting Sb atoms for one or two Si atoms labeled *D*, hence exhibiting Sb coverages of 1.25 ML and 1.5 ML, respectively. In both structures, the modification of the atom positions leads to bond lengths between surface atoms as expected for a largely relaxed surface with slight surface strain only. The bond length between Sb atoms (e.g., in Sb-Sb dimers) is 2.92 Å, which agrees with the bond length of 2.90 Å in rhombohedral Sb crystals.[25] The calculated bonding configuration and the bond lengths for an Sb adatom-tetramer reconstruction are shown in Fig. 10.

The Sb adatom-tetramer reconstruction consists of one Sb tetramer and two Sb adatoms within a (2×2) unit cell corresponding to a Sb coverage of 1.5 ML. According to the DFT calculations, the bonds lengths within Sb tetramers, as indicated in Fig. 10, have values between 2.88 Å and 2.91 Å. The bond lengths between Sb adatoms and adjacent Si atoms as well as between Si(001)-like and Si(111)-like atoms point to slight surface strain. As will be accounted for below, the bonding configuration of the (2×2) Sb tetramer reconstruction, which exhibits a coverage of 2 ML, is not discussed in detail here.

A comparison between the calculated and experimentally determined Fourier coefficients (shown in Table I) yields that the XSW data cannot be explained by the presence of any of the (2×2) reconstructions alone. Therefore, we determined mixtures of surface reconstructions by using the calculated Fourier coefficients of the different reconstructions as input parameters for a least-squares algorithm in which the resulting Fourier coefficients of the phase mixtures were fitted to the XSW data. The relative contributions of the investigated reconstructions were used as free parameters. Also, Debye-Waller factors were implemented. We estimated averaged values of 0.95 in (111) and 0.90 in (113) reflection geometry, respectively. As for coverages below 0.34 ML, the coherent fraction f_c^{202} was neglected. The errors were determined to at most ±0.06 for all phases.

First of all, we obtained that Sb tetramer reconstructions can be neglected for the surfaces investigated here. The con-

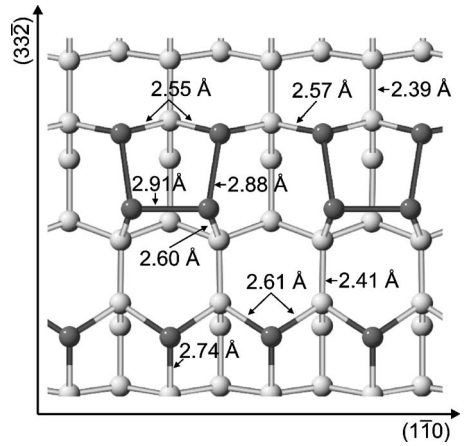

FIG. 10. (2×2) Sb adatom-tetramer reconstruction as resulting from DFT. Sb atoms are displayed in dark shade and Si atoms in light shade. The bond lengths from Sb tetramer atoms to adjacent Si atoms vary within 2.55 Å and 2.61 Å. The bond lengths between Sb tetramer atoms vary between 2.88 Å and 2.91 Å. The bonds between Si(001)-like and Si(111)-like atoms have a length of 2.41 Å and between Sb adatoms and Si(111)-like atoms, a length of 2.74 Å.

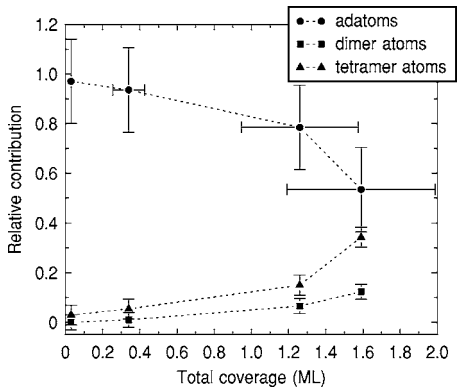

FIG. 11. Contribution of Sb adsorption sites to the surface coverage as resulting from least-squares fit calculations for mixtures of different reconstruction patterns.

tribution of this reconstruction was calculated to values below 0.02, which is expected from the large difference between the calculated Fourier coefficients for this structure and the experimentally determined values shown in Table I.

In order to evaluate the course of occupation of different adsorption sites, the calculated surface mixtures are evaluated site specifically, which is shown in Fig. 11.

For samples with coverages below 0.34 ML, the adsorbate structure is dominated by adatom sites, as the contribution of all other sites can be regarded as zero within the accuracy of the measurements. At higher coverages, the relative contribution of Sb adatom sites decreases, prevalently in benefit of Sb tetramer atoms. At a coverage of 1.26 ML, the contribution of Sb on dimer sites increases only slightly to 0.07, but the contribution of tetramer sites is increased to 0.15. This trend continues at a coverage of 1.59 ML, as Sb dimer atoms have a contribution of 0.12 and tetramer atoms of 0.34. Hence, Sb adsorption sites are occupied successively.

Having established the Sb adatom site at low Sb coverages and having described the surface structure at higher Sb coverages as a complex mixture of (2×2) phases with Sb adatoms, dimers, and tetramers, a scenario for the long-range order that was observed by LEED at annealing above 650 °C may be proposed: We suggest that Sb atoms that are part of dimers or tetramers desorb preferentially as compared to Sb adatoms. With a preference for dissociation of Sb compounds next to vacancies resulting from previous desorption processes, vacancy rows are formed leading to a $(1\times n)$ superstructure.

V. CONCLUSION

We have investigated the adsorption of Sb on the Si(113) surface. A structural phase diagram was established with LEED and XPS by deposition of Sb at RT and subsequent annealing. The LEED patterns showed an Sb-induced (1×2) periodicity between 500 °C and 690 °C. For annealing temperatures between 690 °C and 790 °C various $(1\times n)$ reconstructions occur, which we attribute to the formation of Sb vacancy rows in $[1\bar{1}0]$ direction.

XSW measurements for Sb coverages between 0.03 ML and 1.59 ML were performed in (113), (111), and (202) Bragg reflections. The XSW analysis supported by DFT calculations yields the Sb adatom site as the key structural element for Sb-induced surface reconstructions of Sb on Si(113). At very low coverages, this site can be prevalently found in accordance with the observed LEED patterns. High tensile surface strain favors the formation of interstitial dimers, consisting of Si or Sb atoms as already observed at a coverage of 0.34 ML. At higher coverages, a complex mixture of Sb adatoms, dimers, and tetramers is found, tending toward a (2×2) Sb adatom-tetramer reconstruction. Thus, Sb adsorption sites are occupied subsequently.

The combination of XSW measurements and DFT calculations allowed us to quantitatively determine the contribution of several adsorption sites in complex mixtures of surface phases.

ACKNOWLEDGMENTS

We kindly acknowledge the authors of the PWscf package (Ref. 16), which was used for the DFT calculations.

*Corresponding author. Electronic address: siebert@ifp.uni-bremen.de

[1] M. Copel, M. C. Reuter, E. Kaxiras, and R. M. Tromp, Phys. Rev. Lett. **63**, 632 (1989).
[2] F. K. LeGoues, M. Copel, and R. M. Tromp, Phys. Rev. B **42**, 11690 (1990).
[3] M. Horn-von Hoegen, M. Copel, J. C. Tsang, M. C. Reuter, and R. M. Tromp, Phys. Rev. B **50**, 10811 (1994).
[4] H.-J. Müssig, J. Dąbrowski, K.-E. Ehwald, P. Gaworzewski, A. Huber, and U. Lambert, Microelectron. Eng. **56**, 195 (2001).
[5] G. Wolff, H.-J. Müssig, J. Dąbrowski, W. Arabczyk, and S. Hinrich, Surf. Sci. **357–358**, 667 (1995).
[6] J. Dąbrowski, H.-J. Müssig, G. Wolff, and S. Hinrich, Surf. Sci. **411**, 54 (1998).
[7] K. S. An, C. C. Hwang, C.-Y. Park, and A. Kakizaki, Jpn. J. Appl. Phys., Part 1, **39**, 2771 (2000).
[8] T. Gog, A. Hille, D. Bahr, and G. Materlik, Rev. Sci. Instrum. **66**, 1522 (1995).
[9] B. W. Batterman and H. Cole, Rev. Mod. Phys. **36**, 681 (1964).
[10] J. Zegenhagen, G. Materlik, and W. Uelhoff, J. X-Ray Sci. Technol. **2**, 214 (1990).
[11] J. Zegenhagen, Surf. Sci. Rep. **18**, 202 (1993).
[12] W. Kern, Semicond. Int. **7**, 94 (1984).
[13] W. Ranke, Phys. Rev. B **41**, 5243 (1990).
[14] P. Hohenberg and W. Kohn, Phys. Rev. **136**, B864 (1964).
[15] W. Kohn and L. J. Sham, Phys. Rev. **140**, A1133 (1965).
[16] S. Baroni, A. D. Corso, S. de Gironcoli, and P. Giannozzi, http://www.pwscf.org
[17] G. B. Bachelet, D. R. Hamann, and M. Schlüter, Phys. Rev. B **26**, 4199 (1982).

[18] X. Gonze, R. Stumpf, and M. Scheffler, Phys. Rev. B **44**, 8503 (1991).
[19] D. M. Ceperley and B. J. Alder, Phys. Rev. Lett. **45**, 566 (1980).
[20] J. P. Perdew and A. Zunger, Phys. Rev. B **23**, 5048 (1981).
[21] H. J. Monkhorst and J. D. Pack, Phys. Rev. B **13**, 5188 (1976).
[22] S. Andrieu, J. Appl. Phys. **69**, 1366 (1991).
[23] J. C. Woicik, T. Kendelewicz, K. E. Miyano, C. E. Bouldin, P. L. Meissner, P. Pianetta, and W. E. Spicer, Phys. Rev. B **43**, 4331 (1991).
[24] A. Hirnet, K. Schroeder, S. Blügel, X. Torrelles, M. Albrecht, B. Jenichen, M. Gierer, and W. Moritz, Phys. Rev. Lett. **88**, 226102 (2002).
[25] L. E. Sutton, *Table of Interatomic Distances and Configuration in Molecules and Ions*, Supplement 1956–1959, Special publication No. 18 (Chemical Society, London, 1965).